

# Chapter 4

## Incoherent Digital Holographic Microscopy with Coherent and Incoherent Light

Joseph Rosen and Gary Brooker

**Abstract** Holography is an attractive imaging technique as it offers the ability to view a complete three-dimensional volume from one image. However, holography is not widely applied to the regime of fluorescence microscopy, because fluorescent light is incoherent and creating holograms requires a coherent interferometer system. We review two methods of generating digital Fresnel holograms of three-dimensional microscopic specimens illuminated by incoherent light. In the first method, a scanning hologram is generated by a unique scanning system in which Fresnel zone plates (FZP) are created by a coherently illuminated interferometer. In each scanning period, the system produces an on-axis Fresnel hologram. The twin image problem is solved by a linear combination of at least three holograms taken with three FZPs with different phase values. The second hologram reviewed here is the Fresnel incoherent correlation hologram. In this motionless holographic technique, light is reflected from the 3-D specimen, propagates through a spatial light modulator (SLM), and is recorded by a digital camera. Three holograms are recorded sequentially, each for a different phase factor of the SLM function. The three holograms are superposed in the computer, such that the result is a complex-valued Fresnel hologram that does not contain a twin image. When these two types of hologram are reconstructed in the computer, the 3-D properties of the specimen are revealed.

### 4.1 Introduction

Holographic imaging offers a reliable and fast method to capture the complete 3-D information of the scene from a single perspective. Commonly, there are two phases in the process of holography, namely, the hologram generation and its reconstruction. Usually in the first phase, light from an object is recorded on a certain

---

J. Rosen (✉)

Department of Electrical and Computer Engineering, Ben-Gurion University of the Negev,  
P.O. Box 653, Beer-Sheva 84105, Israel  
e-mail: rosen@ee.bgu.ac.il

holographic medium, whereas in the second phase, an image is reconstructed from the hologram in front of the viewer's eyes. The interaction between holography and the digital world of computers can take place in both phases: in the object acquisition and in the image reconstruction. Basically, there are two methods to generate a hologram, optically or by computers, and there are two methods to reconstruct an image from a hologram, optically or in a computer. The term computer-generated hologram is usually used to indicate the hybrid method in which a hologram is synthesized from computer-generated objects but the reconstruction of the hologram is carried out optically. The term digital hologram (sometimes called electronic hologram) specifies the other hybrid option, in which the hologram is generated optically from real-world objects, by some kind of beam interferences, then digitally processed and reconstructed in the computer. Therefore, in this review, the term incoherent digital hologram means that incoherent light beams reflected or emitted from real existing objects are recorded by a detecting device and digitally processed to yield a hologram. This hologram is reconstructed in the computer, whereas 3-D images appear on the computer's screen. The coherent optical recording is not applicable for the incoherent optics because interference between reference and object incoherent beams cannot occur. Therefore, different holographic acquisition methods should be employed for generating an incoherent digital hologram.

The oldest methods of recording incoherent holograms have made use of the property that every incoherent object is composed of many source points, each of which is self-spatial coherent and therefore can create an interference pattern with light coming from the point's mirrored image. Under this general principle, there are various types of holograms [1–8], including Fourier [2, 6] and Fresnel holograms [3, 4, 8]. The process of beam interfering demands high levels of light intensity, extreme stability of the optical setup, and relatively narrow bandwidth light source. These limitations have prevented holograms from becoming widely used for many practical applications. More recently, three groups of researchers have proposed computing holograms of 3-D incoherently illuminated objects from a set of images taken from different points of view [9–12]. This method, although it shows promising prospects, is relatively slow since it is based on capturing tens of scene images from different view angles. Another method is called scanning holography [13–17], in which a pattern of Fresnel zone plates (FZPs) scans the object such that at each and every scanning position, the light intensity is integrated by a point detector. The overall process yields a Fresnel hologram obtained as a correlation between the object and FZP patterns.

This review concentrates on two techniques of incoherent digital holography that we have been involved recently with its development [17–21]. These two methods are different from each other and they are based on different physical principles. There are only two common aspects that exist in these two methods. First, the system's input signal is always an incoherent light reflected or emitted from a certain 3-D scene. Second, the final product from the two methods is a digital Fresnel hologram.

## 4.2 General Properties of Fresnel Holograms

The type of hologram discussed in this review is the digital Fresnel hologram, which means that a hologram of a single point has the form of the well-known Fresnel zone plate (FZP). The axial location of the object point is encoded by the Fresnel number of the FZP, which is the technical term for the quantity of the rings density in the FZP.

To understand the operation principle of any general Fresnel hologram, let us look at the difference between regular and Fresnel holographic imaging systems. In classical imaging, image formation of objects at different distances from the lens results in a sharp image at the image plane for objects at only one position from the lens, as shown in Fig. 4.1a. The other objects at different distances from the lens are out of focus. Fresnel holographic system, on the other hand, as depicted in Fig. 4.1b, projects a set of rings known as the FZP onto the plane of the image for each and every point at every plane of the object being viewed. The depth of the points is encoded by the density of the rings such that points that are closer to the system project denser rings than distant points. Because of this encoding method, the 3-D information in the volume being imaged is recorded into the recording medium. Therefore, each plane in the image space reconstructed from a Fresnel hologram is in focus at a different axial distance. The encoding is accomplished by the presence

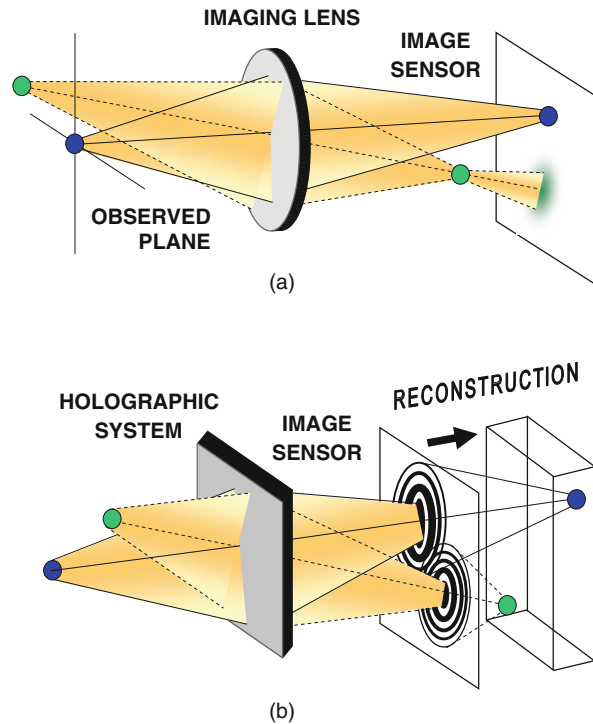


**Fig. 4.1** Comparison of the Fresnel holography principle and conventional imaging. (a) Conventional imaging system. (b) Fresnel holography system

of one of the holographic systems in the image path. Each holographic system, coherent or incoherent, has a different method to project the FZP on the image plane. At this point it should be noted that this graphical description of projecting FZPs by every object's point actually expresses the mathematical 2-D correlation (or convolution) between the object function and the FZP. In other words, the methods of creating Fresnel holograms are different from each other by the way they spatially correlate the FZP with the 3-D scene. Another issue to note is that the correlation should be done with an FZP that is somehow 'sensitive' to the axial locations of the object points. Otherwise, these locations are not encoded into the hologram. The systems described in this review satisfy the condition that the FZP is dependent on the axial distance of each and every object point. This means that indeed points, which are far from the system, project FZP with fewer cycles per radial length than nearby points, and by this condition the holograms can actually image the 3-D scene properly.

The FZP is a sum of at least three main functions, a constant bias, a quadratic phase function, and its complex conjugate. The object function is actually correlated with all these three functions. However, the useful information, with which the holographic imaging is realized, is the correlation with just one of the two quadratic phase functions. The correlation with the other quadratic phase function induces the well-known twin image. This means that the detected signal in the holographic system contains three superposed correlation functions, whereas only one of them is the required correlation between the object and the quadratic phase function. Therefore, the digital processing of the detected signal should contain the ability to eliminate the two unnecessary terms.

The definition of Fresnel hologram is any hologram that contains at least, a correlation (or convolution) between an object function and a quadratic phase function. Moreover, the quadratic phase function must be parameterized according to the axial distance of the object points from the detection plane. In other words, the number of cycles per radial distance of each quadratic phase function in the correlation is dependent on the  $z$  distance of each object point. Formally, a hologram is called Fresnel hologram if its distribution function contains the following term:

$$H(u, v) = \iiint g(x, y, z) \exp \left[ i \frac{2\pi\beta}{z} \left[ (u-x)^2 + (v-y)^2 \right] \right] dx dy dz \quad (4.1)$$

where  $g(x, y, z)$  is the 3-D object function and  $\beta$  is a constant. Indeed, in (4.1) the phase of the exponent is dependent on  $z$ , the axial location of the object. In case the object is illuminated by coherent wave,  $H(u, v)$  given by (4.1) is the complex amplitude of the coherent electromagnetic field directly obtained, under the paraxial approximation [22], by a free space propagation from the object to the detection plane. However, we deal here with incoherent illumination, for which alternative methods to the free propagation should be applied. In fact, in this review we describe two such methods to get the desired correlation with the quadratic phase function given in (4.1), and these methods indeed operate under incoherent illumination.

The more mature technique among the two, and the one that is extensively discussed in the literature, is the scanning holography, pioneered by Poon [13–16]. There are already a textbook [15] and at least one review article [16] on scanning holography. Therefore, in the next section we only summarize briefly the fundamental principles of the classical scanning holography. However, we enlighten a more recent, and less known technique of the scanning holography, called homodyne scanning holography, which we have been involved with its development recently [17].

The second proposed incoherent digital hologram is dubbed Fresnel incoherent correlation hologram (FINCH) [18–21]. The FINCH is actually based on a single-channel on-axis incoherent interferometer. Like any Fresnel holography, in the FINCH the object is correlated with an FZP, but the correlation is carried out without any movement and without multiplexing the image of the scene. Section 4.4 reviews the latest developments of the FINCH in the field of holography and microscopy.

### 4.3 Scanning Holography

Scanning holography [13–17] has demonstrated the ability to produce a Fresnel hologram of the incoherent light emission distributed in a 3-D structure. As mentioned above, the definition of Fresnel hologram is any hologram that contains at least a correlation (or convolution) between an object function and a quadratic phase function. In scanning holography, the required correlation is performed by a mechanical movement. More specifically, a certain pattern, which is the above-mentioned FZP, is projected on the observed object, whereas the FZP moves at a constant velocity relative to the object (or the object moves relative to the FZP). During the movement, the product between the FZP and the object is summed by a lens onto a point detector in discrete times. In other words, the pattern of the FZP scans the object and at each and every scanning position the light intensity is integrated by the detector. The resulting electric signal is a sampled version of the 2-D correlation between the object and the FZP. The dependence of the FZP in the axial position of object points is achieved by interfering two mutually coherent, monochromatic, laser spherical waves on the object surface. The number of cycles per radial distance in each of the spherical waves is dependent on their axial interference location. Since these beams interfere on the object, the axial distance of each object point is stored in the hologram due to the fact that each point is correlated with an FZP the cycle density of which is dependent on the point's 3-D location. Classic scanning holograms [13–16] have been recorded by a heterodyne interferometer in which the holographic information has been encoded on a high carrier frequency. Such method suffers from several drawbacks. On the one hand, trying to keep the scanning time as short as possible requires using carrier frequencies, which may be higher than the bandwidth limit of some, or all of the electronic devices in the system. On the other hand, working with a carrier frequency that is lower than the system limitation extends the scanning time far beyond the minimal time needed

to capture the holographic information according to the sampling theorem. Long scanning times limit the system from recording dynamical scenes. In the scanning holography described in [17], the required correlation is performed by scanning the object with a set of frozen-in-time FZP patterns. In this modified system, the hologram is recorded without temporal carrier frequency, using a homodyne interferometer. This offers an improved method of 3-D imaging that can be applied to incoherent imaging in general and to fluorescence microscopy in particular. As mentioned above, the FZP is created by interference of two coherent spherical waves. As shown in Fig. 4.2, the interference pattern is projected on the specimen, scans it in 2-D, and the reflected light from the specimen is integrated on a detector. Due to the line-by-line scanning by the FZP along the specimen, the one-dimensional detected signal is composed of the entire lines of the correlation matrix between the object function and the FZP. In the computer, the detected signal is reorganized in the shape of a 2-D matrix, the values of which actually represent the Fresnel hologram of the specimen. The specimen we consider is 3-D, and its 3-D structure is stored in the hologram by the effect that during the correlation the number of cycles per radial distance of the FZP contributed from a distant object point is slightly smaller than the number of cycles per radial distance of the FZP contributed from a closer object point.

As mentioned above, the FZP is the intensity pattern of the interference between two spherical waves given by

$$\begin{aligned}
 F(x, y, z) &= Ap(x, y) \left\{ 2 + \exp \left[ \frac{i\pi}{\lambda(z_0 + z)} (x^2 + y^2) + i\theta \right] + \exp \left[ \frac{-i\pi}{\lambda(z_0 + z)} (x^2 + y^2) - i\theta \right] \right\} \\
 &\hspace{15em} (4.2)
 \end{aligned}$$

where  $p(x, y)$  is a disk function with diameter  $D$  that indicates the limiting aperture on the projected FZP,  $A$  is a constant,  $\theta$  is the phase difference between the two spherical waves, and  $\lambda$  is the wavelength of the coherent light source. The constant  $z_0$  indicates that at a plane  $z = 0$ , there is effectively interference between two spherical waves, one emerging from a point at  $z = -z_0$  and the other converging

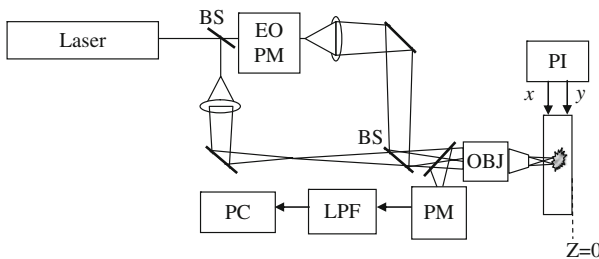


**Fig. 4.2** Optical setup of the homodyne scanning holography system: EOPM, electro-optic phase modulator introducing a phase difference between the two beams; BS, beam splitter; PI, piezo X-Y stage; OBJ, objective; PM, photomultiplier tube detector; LPF, lowpass filter; PC, personal computer

to a point at  $z = z_0$ . This does not necessarily imply that these particular spherical waves are exclusively needed to create the FZP. For a 3-D object  $S(x, y, z)$ , the correlation with the FZP of (4.2) is

$$\begin{aligned}
 H(x, y) = & S(x, y, z) * F(x, y, z) dz = \int S(x, y, z) * p(x, y) dz \\
 & + \iiint S(x', y', z') p(x' - x, y' - y) \\
 & \times \exp \left\{ \frac{i\pi [(x' - x)^2 + (y' - y)^2]}{\lambda(z_0 + z')} + i\theta \right\} dx' dy' dz' \\
 & + \iiint S(x', y', z') p(x' - x, y' - y) \\
 & \times \exp \left\{ \frac{-i\pi [(x' - x)^2 + (y' - y)^2]}{\lambda(z_0 + z')} - i\theta \right\} dx' dy' dz' \quad (4.3)
 \end{aligned}$$

where the asterisk denotes a 2-D correlation. This correlation result is similar to a conventional Fresnel on-axis digital hologram, and therefore, it suffers from the same problems. Specifically,  $H(x, y)$  of (4.3) contains three terms, which represent the information on three images, namely, the 0th diffraction order, the virtual image, and the real image. Trying to reconstruct the image of the object directly from a hologram of the form of (4.3) would fail because of the disruption originated from two images out of the three. This difficulty is solved here with the same solution applied in a conventional on-axis digital holography. Explicitly, at least three holograms of the same specimen are recorded, where for each one of them an FZP with a different phase value  $\theta$  is introduced. A linear combination of the three holograms cancels the two undesired terms and the remaining is a complex-valued on-axis Fresnel hologram, which contains only the information of the single desired image, either the virtual or the real one, according to our choice. A possible linear combination of the three holograms to extract a single correlation between the object and one of the quadratic phase functions of (4.3) is

$$\begin{aligned}
 H_F(x, y) = & H_1(x, y) [\exp(\pm i\theta_3) - \exp(\pm i\theta_2)] \\
 & + H_2(x, y) [\exp(\pm i\theta_1) - \exp(\pm i\theta_3)] \\
 & + H_3(x, y) [\exp(\pm i\theta_2) - \exp(\pm i\theta_1)] \quad (4.4)
 \end{aligned}$$

where  $H_i(x, y)$  is the  $i$ th recorded hologram of the form of (4.3) and  $\theta_i$  is the phase value of the  $i$ th FZP used during the recording process. The choice between the signs in the exponents of (4.4) determines which image, virtual or real, is kept in the final hologram. If, for instance, the virtual image is kept,  $H_F(x, y)$  is the final complex-valued hologram of the form

$$H_F(x, y) = \int S(x, y, z') * p(x, y) \exp \left[ \frac{-i\pi}{\lambda(z_0 + z')} (x^2 + y^2) \right] dz' \quad (4.5)$$

The function  $H_F(x, y)$  is the final hologram that contains the information of only one image – the 3-D virtual image of the specimen in this case. Such image  $S'(x, y, z)$  can be reconstructed from  $H_F(x, y)$  by calculating in the computer the inverse operation to (4.5) as follows:

$$S'(x, y, z) = H_F(x, y) * \exp\left[\frac{i\pi}{\lambda z} (x^2 + y^2)\right] \quad (4.6)$$

The resolution properties of this imaging technique are determined by the properties of the FZP. More specifically, the FZP diameter  $D$  and the constant  $z_0$  characterize the system resolution in a similar way to the effect of an imaging lens [22]. Suppose the image is a single infinitesimal point at  $z = 0$ , then  $H_F(x, y)$  gets the shape of a quadratic phase function limited by a finite aperture. The reconstructed point image has a transverse diameter of  $1.22\lambda z_0/D$ , which defines the transverse resolution, and an axial length of  $8\lambda z_0^2/D^2$ , which defines the axial resolution. Note also that the width of the FZP's last ring along its perimeter is about  $\lambda z_0/D$ , and therefore the size of the specimen's smallest distinguishable detail is approximately equal to the width of this ring.

As an example of the homodyne scanning hologram, let us describe the experiment from [17]. The setup shown in Fig. 4.2 was built on a standard widefield fluorescence microscope. The specimen was a slide with two pollen grains positioned at different distances from the microscope objective. The microscope objective was an infinity-corrected  $20\times$ ,  $NA = 0.75$ . The slide was illuminated by the FZP created by the interferometer. A laser beam ( $\lambda = 532$  nm) was split into two beams with beam expanders consisting each of a microscope objective and a 12-cm focal-length achromat as a collimating lens. One of the beams passed through an electro-optic phase modulator driven by three (or more) constant voltage values, which induce three (or more) phase difference values between the interfering beams. Note that unlike previous studies [13–16], there is no frequency difference between the two interfering waves since this time we record a hologram with a homodyne interferometer. The two waves were combined by the beam splitter to create an interference pattern in the space of the specimen. The pattern was then reduced in size and projected through the objective onto the specimen. The sample was scanned in a 2-D raster with an  $X$ – $Y$  piezo stage. The data were collected by an acquisition system, and data manipulation was performed by programs written in MATLAB.

The three recorded holograms of the specimen taken with phase difference values of  $\theta_{1,2,3} = 0, \pi/2, \text{ and } \pi$  are shown in Fig. 4.3a–c, respectively. In this figures, the dominant term is the low-frequency term [the first in (4.2)], and therefore, without mixing the three holograms in the linear combination that eliminates the low frequency along with the twin image term, there is no possibility to recover the desired image with a reasonable quality. These three holograms are substituted into (4.4) and yield a complex-valued hologram shown in Fig. 4.4. This time the grating lines are clearly revealed in the phase pattern. The computer reconstruction of two pollen grains along the  $z$ -axis is shown in Fig. 4.5. As can be seen in this figure, different parts of the pollen grains are in focus at different transverse planes.



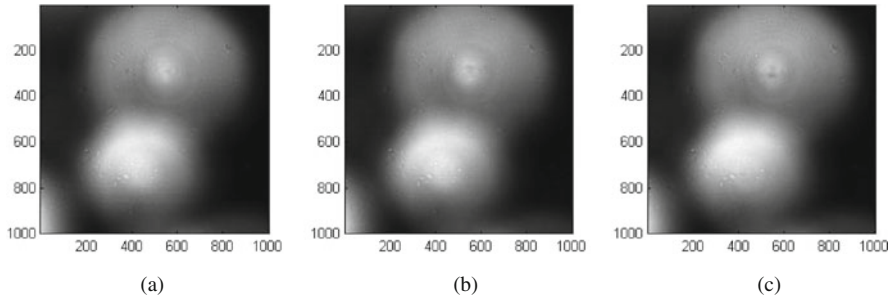


**Fig. 4.3** Three recorded holograms with phase difference between the two interferometers arms of (a) 0, (b)  $\pi/2$ , and (c)  $\pi$ , all obtained from the homodyne scanning holography system

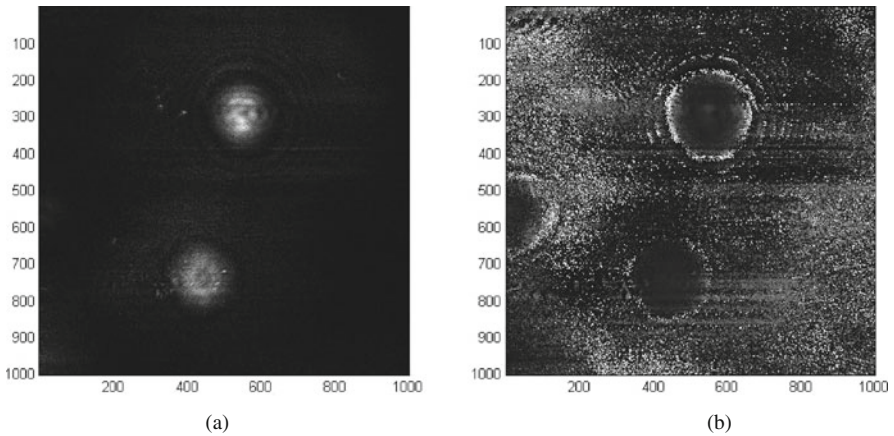


**Fig. 4.4** (a) The magnitude and (b) the phase of the final homodyne scanning hologram

## 4.4 Fresnel Incoherent Correlation Holography

In this section we describe the FINCH – a different method of recording digital Fresnel holograms under incoherent illumination. Various aspects of the FINCH have been described in [18–21], including FINCH of reflected white light [18], FINCH of fluorescence objects [19], FINCHSCOPE [20] – a holographic fluorescence microscope, and finally SAFE [21] – a process of recording incoherent holograms in a synthetic aperture mode. We briefly review these works in this section.

Generally, in the FINCH system, the reflected incoherent light from a 3-D object propagates through a spatial light modulator (SLM) and is recorded by a digital camera. To solve the twin image problem, three holograms are recorded sequentially, each with a different phase factor of the SLM pattern. The three holograms are superposed in the computer such that the result is a complex-valued Fresnel hologram. The 3-D properties of the object are revealed by reconstructing this hologram in the computer.

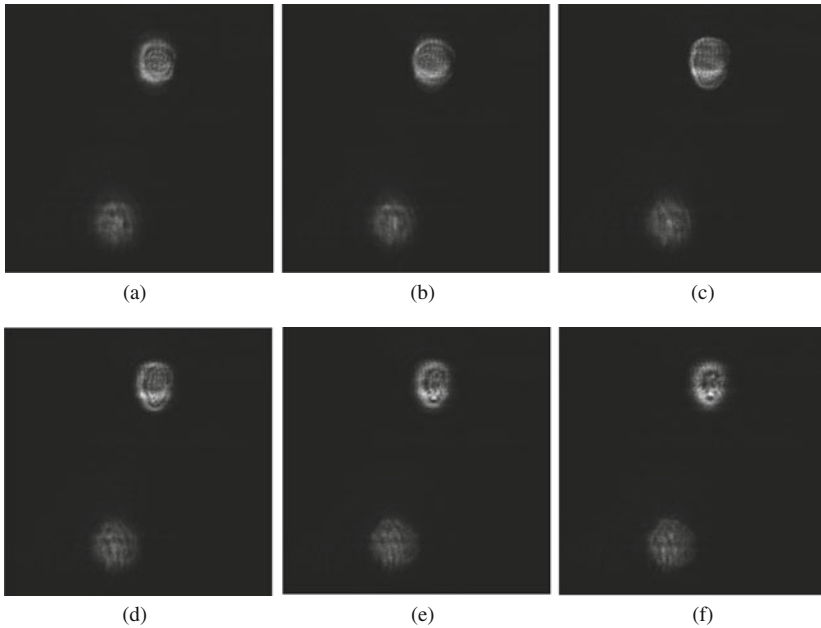


**Fig. 4.5 (a–f)** Various digital reconstructed images along the light propagation axis obtained by digital reconstruction from the hologram of Fig. 4.4

One of the FINCH systems [18] is shown in Fig. 4.6. A white-light source illuminates a 3-D object, and the reflected light from the object is captured by a CCD camera after passing through a lens  $L$  and an SLM. In general, such a system can be analyzed as an incoherent correlator, where the SLM function is considered as a part of the system's transfer function. However, we find it easier to regard the system as an incoherent interferometer, where the grating displayed on the SLM is considered as a beam splitter. As is common in such cases, we analyze the system by following its response to an input object of a single infinitesimal point. Knowing the system's point spread function (PSF) enables one to realize the system operation for any general object. Analysis of a beam originated from a narrowband infinitesimal point source is done using Fresnel diffraction theory [22], since such a source is spatially coherent by definition.

A Fresnel hologram of a point object is obtained when the two interfering beams are, for instance, plane and spherical beams. Such a goal is achieved if the SLM's reflection function  $R(x, y)$  is of the form

$$R(x, y) = \frac{1}{2} + \frac{1}{2} \exp \left[ -\frac{i\pi}{\lambda a} (x^2 + y^2) + i\theta \right] = \frac{1}{2} + \frac{1}{2} Q \left( -\frac{1}{a} \right) \exp(i\theta) \quad (4.7)$$

For the sake of shortening, the quadratic phase function is designated by the function  $Q$ , such that  $Q(b) = \exp[i\pi b/\lambda(x^2 + y^2)]$ . When a plane wave hits the

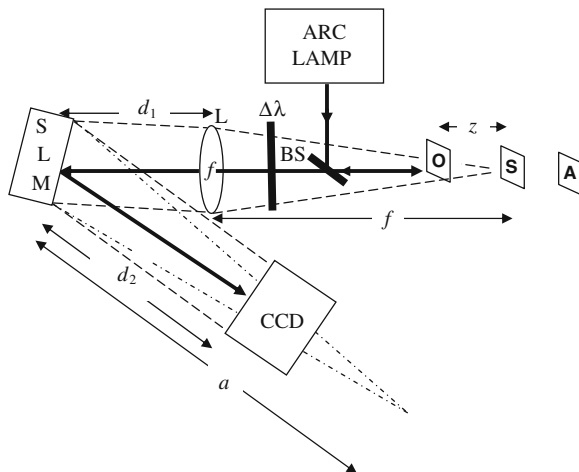


**Fig. 4.6** Schematic of FINCH recorder. BS, beam splitters; SLM, spatial light modulator; CCD, charge-coupled device; L is a spherical lens with  $f = 25$  cm focal length.  $\Delta\lambda$  indicates a chromatic filter with a bandwidth of  $\Delta\lambda = 60$  nm

SLM, the first constant term  $1/2$  in (4.7) represents the reflected plane wave, and the quadratic phase term is responsible for the reflected spherical wave in the paraxial approximation. The angle  $\theta$  plays an important role later in the computation process to eliminate the twin image and the bias term.

A point source located at the point  $(x_s, y_s, z_s)$  a distance  $z_s$  from a spherical positive lens, with  $f$  focal length, induces on the lens plane a diverging spherical wave of the form of  $Q[1/z_s]$ . To simplify the notation we assume that the point sources are located on the front focal plane of the lens, i.e.,  $z_s = f$ . Right after the lens, which has a transmission function of  $Q(-1/f)$ , the complex amplitude is of a tilted plane wave of the form  $C_1(\vec{r}_s)L(-\vec{r}_s/f)$  where the function  $L$  stands for a the linear phase function, such that  $L(\vec{s}) = \exp[i2\pi\lambda^{-1}(s_x x + s_y y)]$ ,  $\vec{r}_s = (x_s, y_s)$ , and  $C_1(\vec{r}_s)$  is a complex constant dependent on the source point's location. After propagating additional distance of  $d_1$  onto the SLM plane, the complex amplitude is the same plane wave besides the constant term. Right after the SLM, with the reflection function given in (4.7), the complex amplitude is equal to  $C_2(\vec{r}_s)L(-\vec{r}_s/f)[1 + \exp(i\theta)Q(-1/a)]$ . Finally, in the CCD plane at a distance  $d_2$  from the SLM, the intensity of the recorded hologram is

$$\begin{aligned}
 I_P(x, y) &= A \left| Q\left(\frac{1}{f}\right) Q\left(\frac{-1}{f}\right) L\left(\frac{-\vec{r}_s}{f}\right) * Q\left(\frac{1}{d_1}\right) \right. \\
 &\quad \times \left. \left[ 1 + \exp(i\theta) Q\left(\frac{-1}{a}\right) \right] * Q\left(\frac{1}{d_2}\right) \right|^2 \\
 &= A \left| L\left(\frac{-\vec{r}_s}{f}\right) \left[ 1 + \exp(i\theta) Q\left(\frac{-1}{a}\right) \right] * Q\left(\frac{1}{d_2}\right) \right|^2 \quad (4.8)
 \end{aligned}$$

where  $A$  is a constant. The result of  $I_P(x, y)$ , after calculating the square magnitude in (4.8), is the PSF for any source point located at any point  $(x_s, y_s)$  on the front focal plane of the lens, as follows:

$$I_P(x, y) = A_o \left( 2 + \exp \left\{ \frac{i\pi}{\lambda(a-d_2)} \left[ \left( x - \frac{d_2 x_s}{f} \right)^2 + \left( y - \frac{d_2 y_s}{f} \right)^2 \right] + i\theta \right\} + \exp \left\{ \frac{-i\pi}{\lambda(a-d_2)} \left[ \left( x - \frac{d_2 x_s}{f} \right)^2 + \left( y - \frac{d_2 y_s}{f} \right)^2 \right] - i\theta \right\} \right) \quad (4.9)$$

The reconstruction distance of the point image from an equivalent optical hologram is  $z_r = a - d_2$ , although in the present case the hologram is of course digital, and the reconstruction is done by the computer. Note that  $z_r$  is obtained specifically in the case that one of the phase masks on the SLM is constant. This choice is used in all the FINCH experiments because practically the fill factor of the SLM is less than 100%, and therefore the constant phase modulation inherently exists in the SLM. Consequently, choosing two diffractive lenses could cause unwanted three, instead of two, waves mixing on the hologram plane, one wave due to the constant phase and the other two from the two different diffractive lenses.

Equation (4.9) is the expression of the transparency function of a hologram created by an object point and recorded by a FINCH system. This hologram has several unique properties. The transverse magnification  $M_T$  is expressed as  $M_T = \partial x_r / \partial x_s = d_2 / f$  for an object located on the front focal plane, and  $M_T = d_2 / z_s$  for any other plane.

For a general 3-D object  $g(x_s, y_s, z_s)$  illuminated by a narrowband incoherent illumination, the intensity of the recorded hologram is an integral of the entire PSF given in (4.9), over all the object intensity  $g(x_s, y_s, z_s)$ , as follows:

$$H(x, y) \cong A_o \left( C + \iiint g(x_s, y_s, z_s) \exp \left\{ \frac{i\pi}{\lambda\gamma(z_s)} \left[ \left( x - \frac{d_2 x_s}{z_s} \right)^2 + \left( y - \frac{d_2 y_s}{z_s} \right)^2 \right] + i\theta \right\} dx_s dy_s dz_s + \iiint g(x_s, y_s, z_s) \exp \left\{ \frac{-i\pi}{\lambda\gamma(z_s)} \left[ \left( x - \frac{d_2 x_s}{z_s} \right)^2 + \left( y - \frac{d_2 y_s}{z_s} \right)^2 \right] - i\theta \right\} dx_s dy_s dz_s \right) \quad (4.10)$$

where  $\gamma(z_s)$ , the reconstruction distance of each object point, is a complicated expression calculated from (4.8), but this time without the special assumption of  $z_s = f$ .

Besides a constant term  $C$ , (4.10) contains two terms of correlation between an object and a quadratic phase,  $z_s$ -dependent, function, which means that the recorded hologram is indeed a Fresnel hologram. In order to remain with a single correlation term out of the three terms given in (4.10), we again follow the usual procedure of on-axis digital holography [17–21]. Three holograms of the same object are recorded each of which with a different phase constant  $\theta$ . The final hologram  $H_F$  is a superposition according to (4.4).

A 3-D image  $g'(x, y, z)$  can be reconstructed from  $H_F(x, y)$  by calculating the Fresnel propagation formula, as follows:

$$g'(x, y, z) = H_F(x, y) * \exp\left[\frac{i\pi}{\lambda z} (x^2 + y^2)\right] \quad (4.11)$$

The system shown in Fig. 4.6 was used to record the three holograms [18]. The SLM (Holoeye HEO 1080P) is phase-only, and as so, the desired function given by (4.7) cannot be directly displayed on this SLM. To overcome this obstacle, the phase function  $Q(-1/a)$  is displayed randomly on only half of the SLM pixels. These pixels were represented in the second term of (4.7), whereas the rest of the pixels representing the first constant term in (4.7) were modulated with a constant phase. The randomness in distributing the two phase functions has been required because organized nonrandom structure produces unnecessary diffraction orders, and therefore results in lower interference efficiency. The pixels were divided equally, half to each diffractive element, to create two wave fronts with equal energy. By this method the SLM function becomes a good approximation to  $R(x, y)$  of (4.7).

The SLM has  $1920 \times 1080$  pixels in a display of  $16.6 \times 10.2$  mm, where only the central  $1024 \times 1024$  pixels were used for implementing the phase mask. The phase distribution of the three reflection masks displayed on the SLM, with phase constants of  $0^\circ$ ,  $120^\circ$ , and  $240^\circ$ , are shown in Fig. 4.7a–c, respectively. The other specifications of the system of Fig. 4.6 are  $f = 250$  mm,  $a = 430$  mm,  $d_1 = 132$  mm, and  $d_2 = 260$  mm.

Three white-on-black letters each of the size  $2 \times 2$  mm were located at the vicinity of rear focal point of the lens. ‘O’ was at  $z = -24$  mm, ‘S’ was at  $z = -48$  mm, and ‘A’ was at  $z = -72$  mm. These letters were illuminated by a mercury arc lamp. A filter that passed a Poisson-like power spectrum from 574 to 725 nm light with a peak wavelength of 599 nm and a bandwidth (full width at half maximum) of 60 nm was positioned between the beam splitter and the lens L. The three holograms, each for a different phase constant of the SLM, were recorded by a CCD camera and processed by a PC. The final hologram  $H_F(x, y)$  was calculated according to (4.4) and its magnitude and phase distributions are depicted in Fig. 4.7e, f, respectively.

The hologram  $H_F(x, y)$  was reconstructed in the computer by calculating the Fresnel propagation toward various  $z$  propagation distances according to (4.11). Three different reconstruction planes are shown in Fig. 4.7g–i. In each plane, a different letter is in focus as is indeed expected from a holographic reconstruction of an object with a volume.

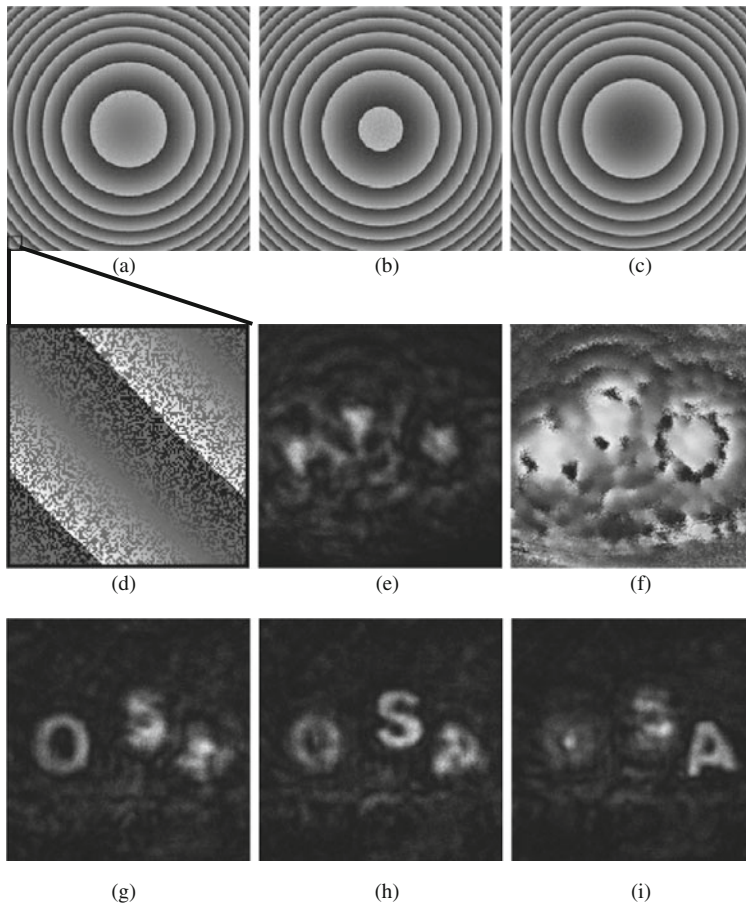


**Fig. 4.7** (a) Phase distribution of the reflection masks displayed on the SLM, with  $\theta = 0^\circ$ , (b)  $\theta = 120^\circ$ , and (c)  $\theta = 240^\circ$ . (d) Enlarged portion of (a) indicating that half (randomly chosen) of the SLM's pixels modulate light with a constant phase. (e) Magnitude and (f) phase of the final on-axis digital hologram. (g) Reconstruction of the hologram of the three letters at the best focus distance of 'O.' (h) Same reconstruction at the best focus distance of 'S' and (i) of 'A'

In [19], the FINCH has been capable of recording multicolor digital holograms from objects emitting fluorescent light. The fluorescent light, specific to the emission wavelength of various fluorescent dyes after excitation of 3-D objects, was recorded on a digital monochrome camera after reflection from the SLM. For each wavelength of fluorescent emission, the camera sequentially records three holograms reflected from the SLM, each with a different phase factor of the SLM's function. The three holograms are again superposed in the computer to create a complex-valued Fresnel hologram of each fluorescent emission without the twin image problem. The holograms for each fluorescent color are further combined in a computer to produce a multicolored fluorescence hologram and 3-D color image.

An experiment showing the recording of a color fluorescence hologram was carried out [19] on the system shown in Fig. 4.8. The phase constants of  $\theta_{1,2,3} = 0^\circ, 120^\circ, \text{ and } 240^\circ$  were introduced into the three quadratic phase functions. The other specifications of the system are  $f_1 = 250 \text{ mm}$ ,  $f_2 = 150 \text{ mm}$ ,  $f_3 = 35 \text{ mm}$ ,  $d_1 = 135 \text{ mm}$ , and  $d_2 = 206 \text{ mm}$ . The magnitude and phase of the final complex hologram, superposed from the first three holograms, are shown in Fig. 4.9a, b, respectively. The reconstruction from the final hologram was calculated using the Fresnel propagation formula of (4.11). The results are shown at the plane of the front face of the front die (Fig. 4.9c), and at the plane of the front face of the rear die (Fig. 4.9d). Note that in each plane a different die face is in focus as is indeed expected from a holographic reconstruction of an object with a volume. The second set of three holograms was recorded via a red filter in the emission filter slider  $F_2$ , which passed 614–640 nm fluorescent light wavelengths with a peak wavelength of 626 nm and a bandwidth of 11 nm (FWHM). The magnitude and phase of the final complex hologram, superposed from the ‘red’ set, are shown in Fig. 4.9e, f, respectively. The reconstruction results from this final hologram are shown in Fig. 4.9g, h at the same planes as shown in Fig. 4.9c, d, respectively. Finally, an additional set of three holograms was recorded with a green filter in emission filter slider  $F_2$ , which passed 500–532 nm fluorescent light wavelengths with a peak wavelength of 516 nm and a bandwidth of 16 nm (FWHM). The magnitude and phase of the final complex hologram, superposed from the ‘green’ set, are shown in Fig. 4.9i, j, respectively. The reconstruction results from this final hologram are shown in Fig. 4.9k, l at the same planes as shown in Fig. 4.9c, d, respectively. Compositions of Fig. 4.9c, g, k and Fig. 4.9d, h, l are depicted in Fig. 4.9m,n, respectively. Note that all the colors in Fig. 4.9 are pseudo-colors. These last results yield a complete

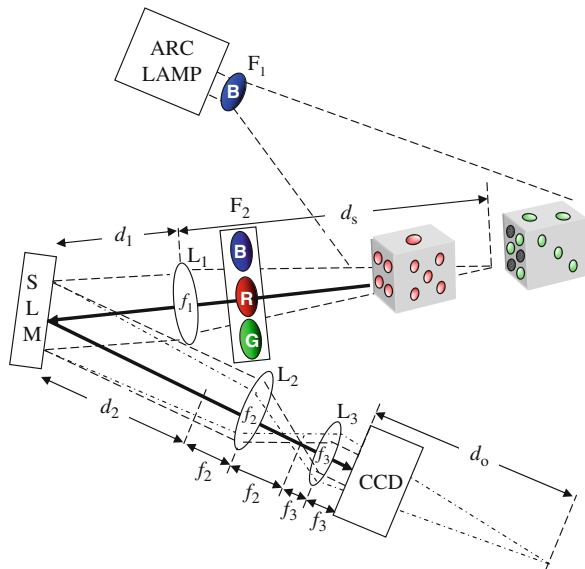


**Fig. 4.8** Schematics of the FINCH color recorder. SLM, spatial light modulator; CCD, charge-coupled device;  $L_1$ ,  $L_2$ ,  $L_3$  are spherical lenses and  $F_1$ ,  $F_2$  are chromatic filters



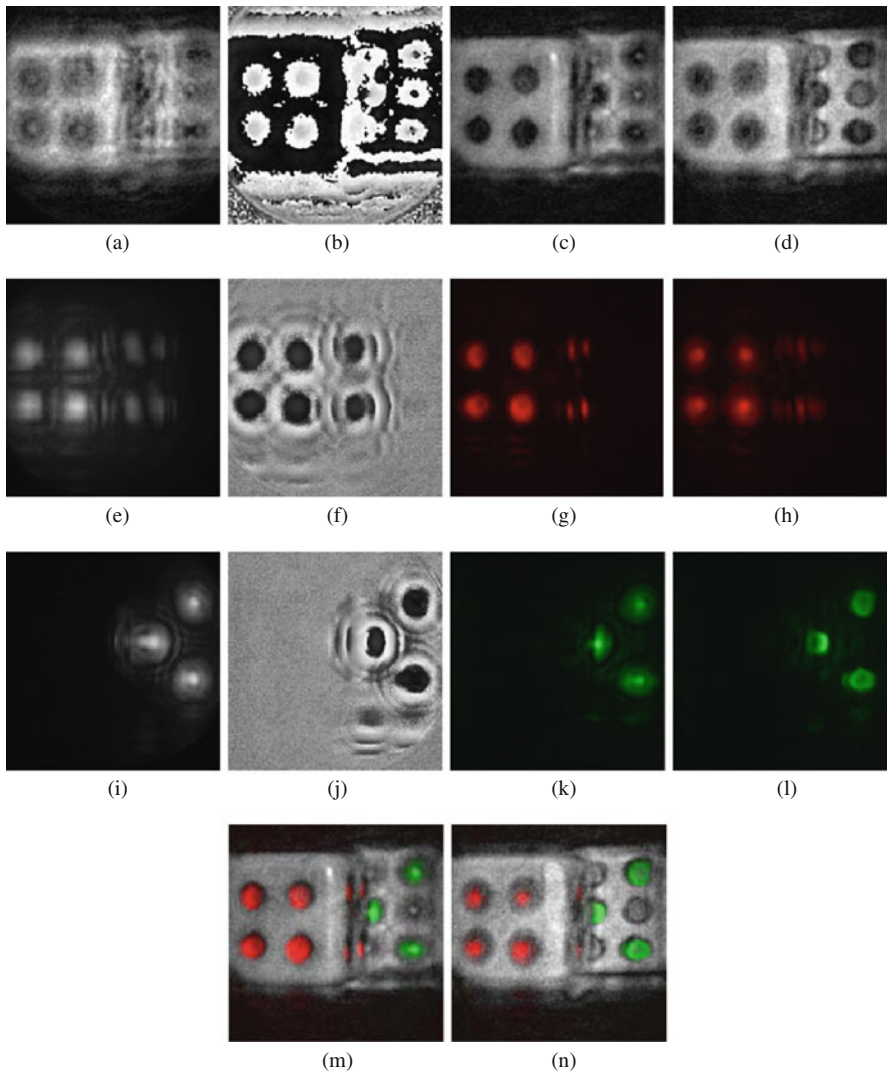


**Fig. 4.9** (a) Magnitude and (b) phase of the complex Fresnel hologram of the dice. Digital reconstruction of the nonfluorescence hologram: (c) at the face of the red dots on the die, and (d) at the face of the green dots on the die. (e) Magnitude and (f) phase of the complex Fresnel hologram of the red dots. Digital reconstruction of the red fluorescence hologram: (g) at the face of the red dots on the die, and (h) at the face of the green dots on the die. (i) Magnitude and (j) phase of the complex Fresnel hologram of the green dots. Digital reconstruction of the green fluorescence hologram: (k) at the face of the red dots on the die and (l) at the face of the green dots on the die. Compositions of (c), (g), (k) and (d), (h), (l) are depicted in (m), (n), respectively



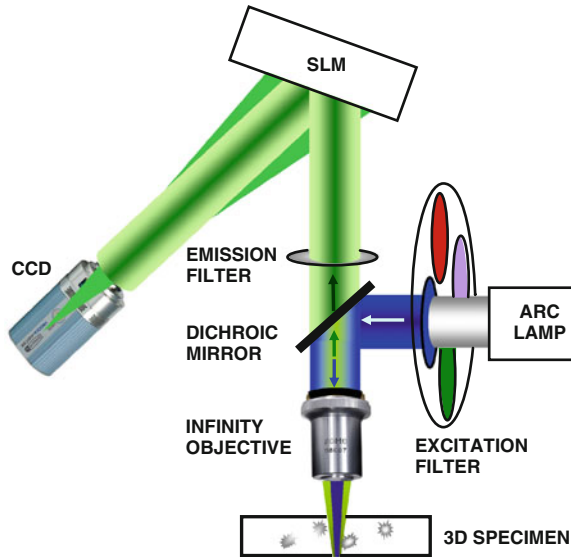


**Fig. 4.10** FINCHSCOPE schematic in upright fluorescence microscope. The upright microscope was modified with a reflective SLM positioned at a tilt angle of  $11^\circ$  to reflect emission light from the objective onto the camera

color 3-D holographic image of the object including the red and green fluorescence. While the optical arrangement in this demonstration has not been optimized for maximum resolution, it is important to recognize that even with this simple optical arrangement, the resolution is good enough to image the fluorescent emissions with good fidelity and to obtain good reflected light images of the dice. Furthermore, in the reflected light images in Fig. 4.9c, m, the system has been able to detect a specular reflection of the illumination from the edge of the front dice.

The next system to be reviewed here is the first demonstration of a motionless microscopy system (FINCHSCOPE) based upon the FINCH, and its use in recording high-resolution 3-D fluorescent images of biological specimens [20]. By using high-numerical-aperture lenses, a spatial light modulator, a charge-coupled device camera, and some simple filters, FINCHSCOPE enables the acquisition of 3-D microscopic images without the need for scanning.

A schematic diagram of the FINCHSCOPE for an upright microscope equipped with an arc lamp source is shown in Fig. 4.10. The beam of light that emerges from an infinity-corrected microscope objective transforms each point of the object being viewed into a plane wave, thus satisfying the first requirement of FINCH [18]. An SLM and a digital camera replace the tube lens, reflective mirror, and other transfer optics normally present in microscopes. Because no tube lens is required, infinity-corrected objectives from any manufacturer can be used. A filter wheel was used to select excitation wavelengths from a mercury arc lamp, and the dichroic mirror holder and the emission filter in the microscope were used to direct light to and from the specimen through infinity-corrected objectives.

The ability of the FINCHSCOPE to resolve multicolor fluorescent samples was evaluated by first imaging polychromatic fluorescent beads. A fluorescence bead slide with the beads separated on two separate planes was constructed. FocalCheck polychromatic beads ( $6\ \mu\text{m}$ ) were used to coat one side of a glass microscope slide and a glass coverslip. These two surfaces were juxtaposed and held together at a distance from one another of  $\sim 50\ \mu\text{m}$  with optical cement. The beads were sequentially excited at 488, 555, and 640 nm center wavelengths (10–30 nm bandwidths) with emissions recorded at 515–535 nm, 585–615 nm, and 660–720 nm, respectively. Figure 4.11a–d shows reconstructed image planes from  $6\ \mu\text{m}$  beads excited at 640 nm and imaged on the FINCHSCOPE with a Zeiss PlanApo  $\times 20$ , 0.75 NA objective. Figure 4.11a shows the magnitude of the complex hologram, which contains all the information about the location and intensity of each bead at every plane in the field. The Fresnel reconstruction from this hologram was selected to yield 49 planes of the image,  $2\ \mu\text{m}$  apart. Two beads are shown in Fig. 4.11b, with only the lower bead exactly in focus. The next image (Fig. 4.11c) is  $2\ \mu\text{m}$  into the field in

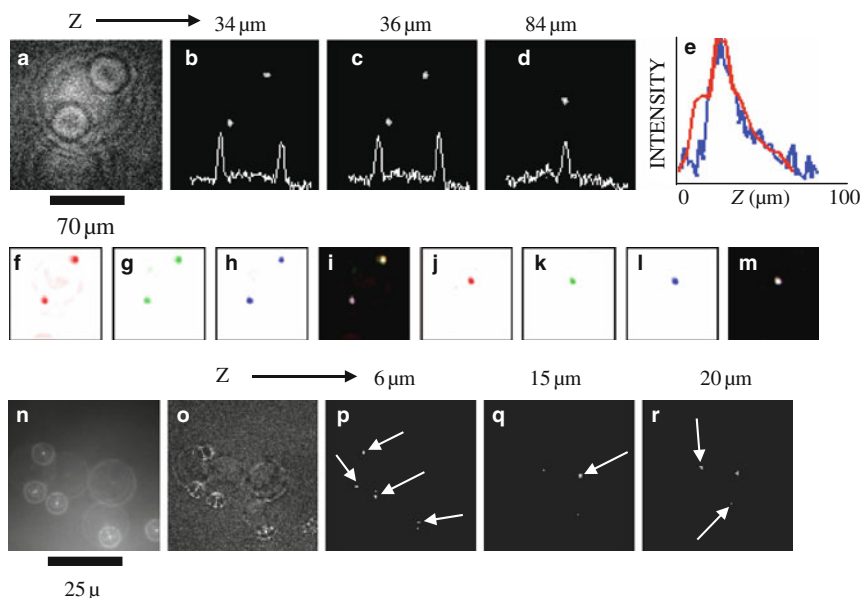


**Fig. 4.11** FINCHSCOPE holography of polychromatic beads. (a) Magnitude of the complex hologram  $6\ \mu\text{m}$  beads. Images reconstructed from the hologram at  $z$  distances of (b)  $34\ \mu\text{m}$ , (c)  $36\ \mu\text{m}$ , and (d)  $84\ \mu\text{m}$ . Line intensity profiles between the beads are shown at the bottom of panels b–d. (e) Line intensity profiles along the  $Z$  axis for the lower bead from reconstructed sections of a single hologram (*blue line*) and from a widefield stack of the same bead (28 sections, *red line*). (f–h) Beads ( $6\ \mu\text{m}$ ) excited at 640, 555, and 488 nm with holograms reconstructed at planes b and (j–l) d. (i, m) are the combined RGB images for planes b and d, respectively. (n–r) Beads ( $0.5\ \mu\text{m}$ ) imaged with a 1.4-NA oil immersion objective: (n) holographic camera image; (o) magnitude of the complex hologram; (p–r) reconstructed image planes 6, 15, and  $20\ \mu\text{m}$ . Scale bars indicate image size

the  $Z$ -direction, and the upper bead is now in focus, with the lower bead slightly out of focus. The focal difference is confirmed by the line profile drawn between the beads, showing an inversion of intensity for these two beads between the planes. There is another bead between these two beads, but it does not appear in Fig. 4.11b or c (or in the intensity profile), because it is  $48\ \mu\text{m}$  from the upper bead; it instead appears in Fig. 4.11d (and in the line profile), which is 24 sections away from the section in Fig. 4.11c. Notice that the beads in Fig. 4.11b, c are no longer visible in Fig. 4.11d. In the complex hologram in Fig. 4.11a, the small circles encode the close beads and the larger circles encode the distant central bead. Figure 4.11e shows that the  $Z$ -resolution of the lower bead in Fig. 4.11b, reconstructed from sections created from a single hologram (blue line), is at least comparable to data from a widefield stack of 28 sections (obtained by moving the microscope objective in the  $Z$ -direction) of the same field (red line). The colocalization of the fluorescence emission was confirmed at all excitation wavelengths and at extreme  $Z$  limits as shown in Fig. 4.11f–m for the  $6\ \mu\text{m}$  beads at the planes shown in Fig. 4.11b, f–i and 4.11d, j–m. In Fig. 4.11n–r,  $0.5\ \mu\text{m}$  beads (TetraSpeck, Invitrogen) imaged with a Zeiss PlanApo  $\times 63$  1.4 NA oil-immersion objective are shown. Figure 4.11n presents one of the holograms captured by the camera and Fig. 4.11o shows the magnitude of the complex hologram. Figure 4.11p–r shows different planes (6, 15, and  $20\ \mu\text{m}$ , respectively) in the bead specimen after reconstruction from the complex hologram of image slices in  $0.5\ \mu\text{m}$  steps. Arrows show the different beads visualized in different  $Z$  image planes. The computer reconstruction along the  $Z$ -axis of a group of fluorescently labeled pollen grains (Carolina Biological slide no. 30-4264) is shown in Fig. 4.12b–e. As is expected from a holographic reconstruction of a 3-D object with volume, any number of planes can be reconstructed. In this example, a different pollen grain was in focus in each transverse plane reconstructed from the complex hologram whose magnitude is shown in Fig. 4.12a. In Fig. 4.12b–e, the values of  $Z$  are 8, 13, 20, and  $24\ \mu\text{m}$ , respectively. A similar experiment was performed with the autofluorescent *Convallaria* rhizome and the results are shown in Fig. 4.12g–j at planes 6, 8, 11, and  $12\ \mu\text{m}$ .

The most recent development in FINCH is a new lensless incoherent holographic system operating in a synthetic aperture mode [21]. Synthetic aperture is a well-known superresolution technique, which extends the resolution capabilities of an imaging system beyond the theoretical Rayleigh limit dictated by the system's actual aperture. Using this technique, several patterns acquired by an aperture-limited system, from various locations, are tiled together to one large pattern, which could be captured only by a virtual system equipped with a much wider synthetic aperture.

The use of optical holography for synthetic aperture is usually restricted to coherent imaging [23–25]. Therefore, the use of this technique is limited only to those applications in which the observed targets can be illuminated by a laser. Synthetic aperture carried out by a combination of several off-axis incoherent holograms in scanning holographic microscopy has been demonstrated by Indebetouw et al. [26]. However, this method is limited to microscopy only, and although it is a technique

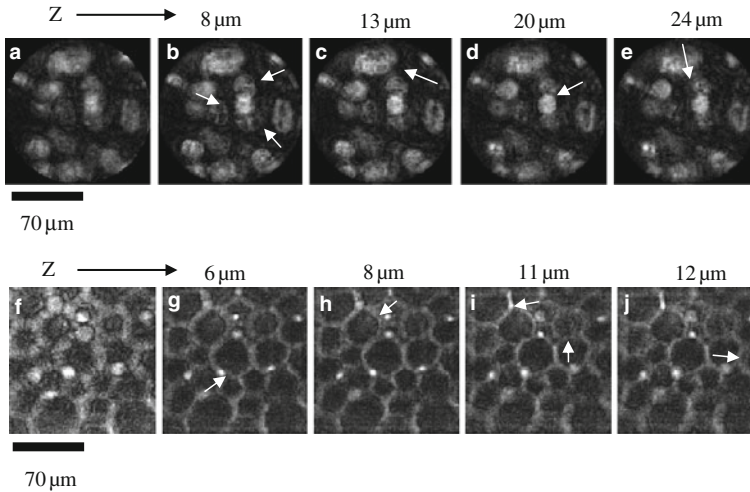


**Fig. 4.12** FINCHSCOPE fluorescence sections of pollen grains and *Convallaria* rhizome. The *arrows* point to the structures in the images that are in focus at various image planes. (**b–e**) Sections reconstructed from a hologram of mixed pollen grains. (**g–j**) Sections reconstructed from a hologram of *Convallaria* rhizome. (**a, f**) Magnitude of the complex holograms from which the respective image planes were reconstructed. Scale bars indicate image sizes

of recording incoherent holograms, a specimen should also be illuminated by an interference pattern between two laser beams.

Our new scheme of holographic imaging of incoherently illuminated objects is dubbed a synthetic aperture with Fresnel elements (SAFE). This holographic lensless system contains a band-pass filter, a polarizer, an SLM, and a digital camera. SAFE has an extended synthetic aperture in order to improve the transverse and axial resolutions beyond the classic limitations. The term synthetic aperture, in the present context, means time (or space) multiplexing of several Fresnel holographic elements captured from various viewpoints by a system with a limited real aperture. The synthetic aperture is implemented by shifting the BPF–polarizer–SLM–camera set, located across the field of view, between several viewpoints. At each viewpoint a different mask is displayed on the SLM, and a single element of the Fresnel hologram is recorded (see Fig. 4.13). The various elements, each of which is recorded by the real aperture system during the capturing time, are tiled together so that the final mosaic hologram is effectively considered as captured from a single synthetic aperture, which is much wider than the actual aperture.

An example of such system with the synthetic aperture, which is three times wider than the actual aperture, can be seen in Fig. 4.13. For simplicity of the demonstration, the synthetic aperture was implemented only along the horizontal axis. In principle, this concept can be generalized for both axes and for any ratio of synthetic to actual apertures. Imaging with the synthetic aperture is necessary for cases where the angular spectrum of the light emitted from the observed object is wider than the numerical aperture of a given imaging system. In SAFE shown in Fig. 4.13,

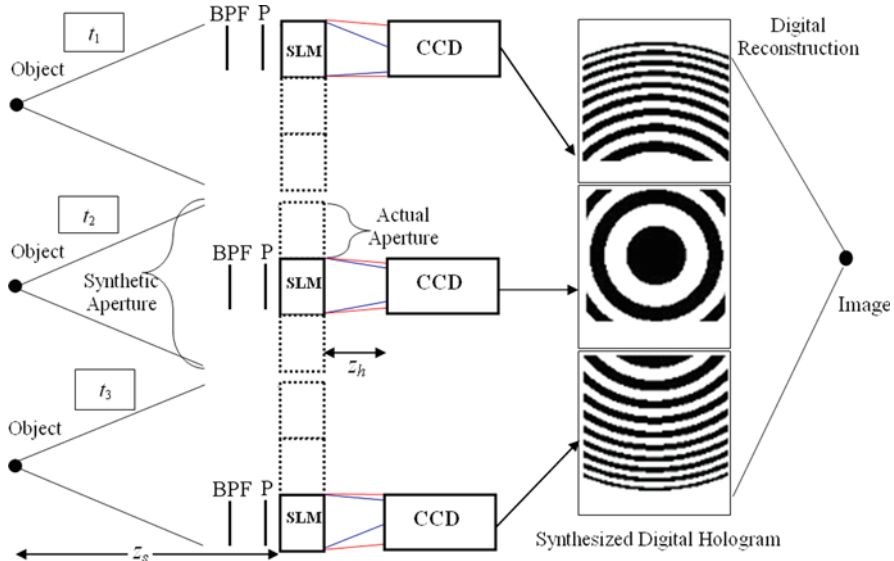


**Fig. 4.13** Scheme of SAFE operating as synthetic aperture radar to achieve superresolution. P indicates polarizer

the SLM and the digital camera move in front of the object. The complete Fresnel hologram of the object, located at some distance from the SLM, is a mosaic of three holographic elements, each of which is recorded from a different position by the system with the real aperture of the size  $A_x \times A_y$ . The complete hologram tiled from the three holographic Fresnel elements has the synthetic aperture of the size  $3 \cdot A_x \times A_y$ , which is three times larger than the real aperture at the horizontal axis.

The method to eliminate the twin image and the bias term is the same as has been used before; three elemental holograms of the same object and for each point of view are recorded, and each of the holograms has a different phase constant of the SLM's phase mask. The final holographic element is a specific superposition of the three recorded elements. The digital reconstruction of the final complex-valued mosaic hologram is conventionally computed by Fresnel back propagation.

SAFE has been tested in the lab by the system shown in Fig. 4.13. The object in this experiment is a binary grating with cycle length of four lines per mm. The distance from the object to the SLM has been 52 cm, and the distance between the phase-only SLM (Holoeye, PLUTO) and the digital camera (E-VISION, EVC6600SAM-GE5) has been 38.5 cm. A 100 W Halogen ARC lamp has been used for objects illumination, and a BPF (with an 80 nm bandwidth surrounding 550 nm central wavelength) has been placed just in front of the SLM. The results of the experiments are summarized in Fig. 4.14. In the first experiment we have recorded a hologram only by the actual aperture without shifting the system, in the setup shown in Fig. 4.13 at the time  $t_2$ . Figure 4.14a shows one of the three masks displayed on the SLM in this experiment. Each of the three masks has one of the three different phase factors:  $0^\circ$ ,  $120^\circ$ , or  $240^\circ$ . As mentioned above, these

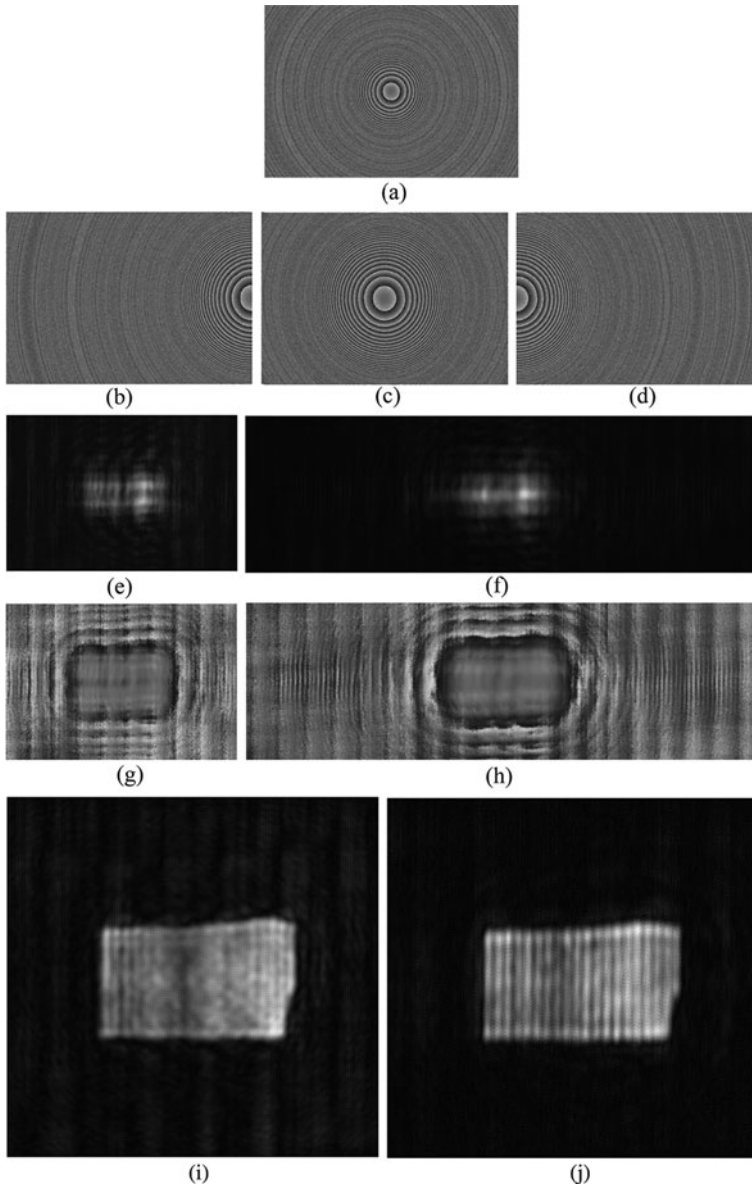


**Fig. 4.14** Results of SAFE for the first object with the real and synthetic apertures. (a) is the phase distribution of the reflection masks displayed on the SLM at  $\theta = 120^\circ$  with the real aperture; (b–d) are the same as (a) using the synthetic aperture; (e) is the magnitude of the final on-axis digital hologram with the real aperture and (f) is the same as (e) with the synthetic aperture; (g) is the phase of the final hologram with the actual aperture and (h) is the phase with the synthetic aperture; (i) is the reconstruction of the hologram of the binary grating at the best focus distance for the real aperture and (j) is for the synthetic aperture

three phase masks with different phase constants are required in order to eliminate the bias term and the twin image from the holographic reconstruction. As stated earlier, another problem with the SLM is that its fill factor is 87%, which means that part of the light is reflected from the SLM without any modulation. In order to avoid the interference of three waves projected on the camera, we have chosen one of the phase elements to be constant. The other phase element has been chosen to be a negative diffractive lens with the shortest focal distance that can be achieved with the SLM having the pixel size of  $8\ \mu\text{m}$ . The shortest focal distance guarantees maximum resolution power for a given aperture size. In the case of the actual aperture ( $1500 \times 1000$  pixels) and the synthetic aperture ( $3000 \times 1000$  pixels), the focal distances have been  $-34\ \text{cm}$  and  $-68\ \text{cm}$ , respectively. The  $NA_{\text{in}}$  is 0.0115 and 0.0231 for the real and synthetic apertures, respectively. The  $NA_{\text{out}}$  is 0.0035 and 0.0044 for the real and synthetic apertures, respectively. Note that the sum of two pure phase functions, i.e., the quadratic phase function  $Q[-1/a]$  and the constant phase function in (4.7), is no longer a pure phase function but a complex function with nonconstant magnitude. Since the SLM is a phase-only modulator, we use the previous method of recording general complex function on a phase-only SLM. Each phase function is distributed randomly among half of the SLM pixels.

The three recorded holograms are superposed according to the same superposition (4.4). Figure 4.14e, g is the magnitude and the phase of the superposed holograms for the object. It can be seen that the resolution along the horizontal direction of the reconstructed image, computed by Fresnel back propagation, is damaged in the sense that the image is lacking the original high-frequency gratings along the horizontal direction because the aperture is too narrow to capture the entire gratings spectral content. This damaged reconstructed image is shown in Fig. 4.14i.

In the SAFE experiment, nine different phase masks have been displayed on the SLM, three for each location of the SLM–camera set: left, central, and right. Each of the masks has an actual aperture of  $1500 \times 1000$  pixels. Each of the three masks at every location has one of the three different phase factors:  $0^\circ$ ,  $120^\circ$ , or  $240^\circ$ . In order to avoid edge effects on the recorded holograms, there is an overlap of 750 pixels among the three actual apertures combining the synthetic aperture. For each location of the system, the three recorded holograms have been superposed as mentioned above. Figure 4.14b–d represents three masks out of nine, each of which has been displayed at a different time and at a different location of the setup along the horizontal axis. The superposed complex-valued holographic element from each system’s viewpoint is stored in the computer. Upon completing the system movement along the entire synthetic aperture, all three holographic elements are tiled to a single mosaic hologram. Figure 4.14f, h represents the magnitude and the phase of the complete mosaic hologram. The reconstruction result of the mosaic hologram, computed by Fresnel back propagation, is depicted in Fig. 4.14j. The binary grating on the observed objects is seen well in the reconstructed images, indicating that the synthetic aperture is wide enough to acquire most of the horizontal spectral information of the objects.



## 4.5 Discussion and Conclusions

We have reviewed two different methods of generating incoherent digital Fresnel holograms. The homodyne scanning holography setup has some advantages over the previous designs of scanning holography. The main advantage is that the overall scanning time can be shorter than the case of heterodyne scanning holography. Also, the proposed system is more immune from noise than previous scanning holography systems because in the homodyne scanning holography, only frozen-in-time FZP patterns scan the object. However, the main limitation of scanning holography – the need for a 2-D scan – does exist in the homodyne version as well. In view of this limitation, the scanning holography, in all of its versions, is considered as the slowest method in capturing the scene among all the methods of digital holography.

The second reviewed hologram, the FINCH, is actually recorded by an on-axis, single-channel, incoherent interferometer. This method inherently does not scan the object, neither in the space nor in the time. Therefore, the FINCH can generate the holograms rapidly without sacrificing the system resolution. This system offers the feature of observing a complete volume from a hologram, potentially enabling objects moving quickly in three dimensions to be tracked. The FINCH technique shows great promise in rapidly recording 3-D information in any scene, independently of the illumination. In addition, we have described a rapid, non-scanning holographic fluorescence microscope that produces in-focus images at each plane in the specimen from holograms captured on a digital camera. This motionless 3-D microscopy technique does not require complicated alignment or a laser. The fluorescence emission can be of relatively wide bandwidth because the optical path difference between the beams is minimal in this single-path device. Although at present each reconstructed section is not completely confocal, 3-D reconstructions free of blur could be created by deconvolution of the holographic sections as is typically carried out in widefield microscopy. Time resolution is currently reduced because three holograms need to be captured sequentially. However, in the future, it will be possible to simultaneously capture all three holograms or to overcome the holographic twin image problem and capture only one hologram, as any of the three holograms contains all the essential 3-D information. In the present studies, the image sections were obtained by a process of first capturing three holograms, computing the image  $z$  sections from the complex hologram and then, in some cases, further enhancing them by deconvolution. This process could be simplified in the future for real-time display of the holographic image, either with a holographic display system or by algorithms that create the enhanced sections and the 3-D representation directly from the single hologram. There is no need for sectioning or scanning or any mechanical movement. Therefore, this system would be expected ultimately to be faster, simpler, and more versatile than existing 3-D microscopy techniques, which rely on pinhole imaging or deconvolution of stacks of widefield images. At present, the FINCHSCOPE is already considerably faster than conventional 3-D sectioning. For example, the total image capture time for the three FINCHSCOPE images of the pollen grains in Fig. 4.12 was just over 1 s, compared with the 30–45 s needed to create a stack of 48 widefield or spinning



disk confocal images. We have also demonstrated fluorescence holography using the high-NA objectives widely used in biological imaging. FINCHSCOPE is able to spatially resolve small beads, biological specimens, and different fluorescence emission colors in  $x$ ,  $y$ , and  $z$  planes with perfect registration. The system provides a simple, flexible, cost-effective, and powerful microscopic platform for 3-D imaging. Our demonstration of this advance in microscopy, based on a new, but simple holographic principle, should open up opportunities in many life science and engineering fields, so that living or fixed specimens may be readily observed in three dimensions and possibly at higher resolution than with currently existing techniques.

## References

1. A.W. Lohmann, Wavefront reconstruction for incoherent objects. *J. Opt. Soc. Am.* **55**, 1555–1556 (1965)
2. G.W. Stroke, R.C. Restrck, III, Holography with spatially noncoherent light. *Appl. Phys. Lett.* **7**, 229–231 (1965)
3. G. Cochran, New method of making Fresnel transforms with incoherent light. *J. Opt. Soc. Am.* **56**, 1513–1517 (1966)
4. P. Peters, Incoherent holograms with a mercury light source. *J. Appl. Phys. Lett.* **8**, 209–210 (1966)
5. H.R. Worthington, Jr., Production of holograms with incoherent illumination. *J. Opt. Soc. Am.* **56**, 1397–1398 (1966)
6. J.B. Breckinridge, Two-dimensional white light coherence interferometer. *Appl. Opt.* **13**, 2760–2762 (1974)
7. A.S. Marathay, Noncoherent-object hologram: Its reconstruction and optical processing. *J. Opt. Soc. Am. A* **4**, 1861–1868 (1987)
8. L.M. Mugnier, G.Y. Sirtat, D. Charlot, Conoscopic holography: Two-dimensional numerical reconstructions. *Opt. Lett.* **18**, 66–68 (1993)
9. Y. Li, D. Abookasis, J. Rosen, Computer-generated holograms of three-dimensional realistic objects recorded without wave interference. *Appl. Opt.* **40**, 2864–2870 (2001)
10. Y. Sando, M. Itoh, T. Yatagai, Holographic three-dimensional display synthesized from three-dimensional Fourier spectra of real-existing objects. *Opt. Lett.* **28**, 2518–2520 (2003)
11. N.T. Shaked, J. Rosen, Multiple-viewpoint projection holograms synthesized by spatially incoherent correlation with broadband functions. *J. Opt. Soc. Am. A* **25**, 2129–2138 (2008)
12. J.-H. Park, M.-S. Kim, G. Baasantseren, N. Kim, Fresnel and Fourier hologram generation using orthographic projection images. *Opt. Exp.* **17**, 6320–6334 (2009)
13. T.-C. Poon, A. Korpel, Optical transfer function of an acousto-optic heterodyning image processor. *Opt. Lett.* **4**, 317–319 (1979)
14. B.W. Schilling, T.-C. Poon, G. Indebetouw, B. Storrie, K. Shinoda, Y. Suzuki, M.H. Wu, Three-dimensional holographic fluorescence microscopy. *Opt. Lett.* **22**, 1506–1508 (1997)
15. T.-C. Poon, *Optical Scanning Holography with MATLAB* (Springer, New York, NY, 2007)
16. T.-C. Poon, Recent progress in optical scanning holography. *J. Hologr. Speckle* **1**, 6–25 (2004)
17. J. Rosen, G. Indebetouw, G. Brooker, Homodyne scanning holography. *Opt. Exp.* **14**, 4280–4285 (2006)
18. J. Rosen, G. Brooker, Digital spatially incoherent Fresnel holography. *Opt. Lett.* **32**, 912–914 (2007)
19. J. Rosen, G. Brooker, Fluorescence incoherent color holography. *Opt. Exp.* **15**, 2244–2250 (2007)
20. J. Rosen, G. Brooker, Non-scanning motionless fluorescence three-dimensional holographic microscopy. *Nat. Photon.* **2**, 190–195 (2008)

21. B. Katz, J. Rosen, Super-resolution in incoherent optical imaging using synthetic aperture with Fresnel elements. *Opt. Exp.* **18**, 962–972 (2010)
22. J.W. Goodman, *Introduction to Fourier Optics*, 2nd edn. (McGraw-Hill, New York, NY, 1996)
23. S.M. Beck, J.R. Buck, W.F. Buell, R.P. Dickinson, D.A. Kozlowski, N.J. Marechal, T.J. Wright, Synthetic-aperture imaging laser radar: Laboratory demonstration and signal processing. *Appl. Opt.* **44**, 7621–7629 (2005)
24. V. Mico, Z. Zalevsky, P. García-Martínez, J. García, Synthetic aperture superresolution with multiple off-axis holograms. *J. Opt. Soc. Am. A* **23**, 3162–3170 (2006)
25. L. Martínez-León, B. Javidi, Synthetic aperture single-exposure on-axis digital holography. *Opt. Exp.* **16**, 161–169 (2008)
26. G. Indebetouw, Y. Tada, J. Rosen, G. Brooker, Scanning holographic microscopy with resolution exceeding the Rayleigh limit of the objective by superposition of off-axis holograms. *Appl. Opt.* **46**, 993–1000 (2007)